Proceedings of IMECE2006
2006 ASME International Mechanical Engineering Congress and Exposition
November 5-10, 2006, Chicago, Illinois, USA

IMECE2006-14399

MODELING AND EXPERIMENTAL VERIFICATION OF TORQUE RIPPLE IN PERMANENT MAGNET DC MOTORS

Benjamin A. Lovett
Graduate Student
School of Mechanical Engineering
Purdue University
West Lafayette, IN 47907
lovett@purdue.edu

George T.-C. Chiu
Associate Professor
School of Mechanical Engineering
Purdue University
West Lafayette, IN 47907
gchiu@purdue.edu

ABSTRACT

In this paper we have developed a simple parametric model based on motor geometries to estimate the torque ripple in permanent-magnet DC (PMDC) motors. Torque ripple is the combined results of many different motor design parameters such as magnetic material properties and geometry as well as rotor slot geometry. As the PMDC motors are being used in more precision applications while being produced at a lower price, the effect of torque ripple is becoming an important issued for precision motion control. The main objective of this study is to identify motor parameters that affect the magnitude of the torque ripples as well as developing a cost effective measuring device for motor vendors. The analytical model focused on the effect of air gap volume on effective magnetic flux and in terms impact the torque generation. The effectiveness of the proposed model was verified by experimental data collected with motors from four large volume motor vendors that meets the same design specification. Sensitivity analysis was also performed to identify the key motor parameters that impacted the magnitude of the torque ripple.

INTRODUCTION

The use of brushed permanent magnet DC (PMDC) motors in machines that are used in precision application has become more common over the years. The reason for this trend is due to an increase in quality and cost effectiveness through advances in manufacturing processes. These advances have not however eliminated a periodic fluctuation of the output torque of the motor which is dependent on angular position and can be termed torque ripple (*TR*). This paper will first discuss a model of the motor developed torque T_D and *TR* and then compare model simulation with experimentally collected data from four different brushed PMDC motor vendors. Finally, the physical parameters of the brushed PMDC motor that is most responsible for *TR* will be identified. Models have previously been developed [1, 2] that calculate the output torque based change in energy with respect to angular position and air gap field distribution and net lateral force acting on rotor teeth. The use of these models and similar models others have suggested methods of reducing torque fluctuations such as varying the width of slots or space between PM's [3], skewing rotor slots [4], notching stator teeth and PM shaping [5], and effects from slot and pole count [6]. These studies and other studies, [7-13], suggest methods for altering the manufacturing process whereas this study will identify the key parameters so that manufacturers are able to focus their design on these parameters and develop motors that contain *TR* of similar magnitude.

NOMENCLATURE

A_a	cross-sectional area of the air gap (m^2)
A_F	cross-sectional area of the ferrous material (m^2)
A_m	cross-sectional area of the permanent magnet (m^2)
B	number of coils in the armature
B_m	remanence flux density (Tesla)
K_T	motor torque constant (Newton-meter/Amp)
K_v	back EMF constant (Volts)
L	self inductance (Henry)
M	mutual inductance (Henry)
N	number of turns in armature coil
N_P	number of permanent magnet poles
N_S	number of slots in the rotor
T_D	developed motor torque (Newton-meter)
TR	torque ripple (Newton-meter)

V_m armature voltage (Volts)
W_T total energy stored (Joules)
W_f energy stored in the electromagnetic field (Joules)
c_m magnet width (m)
c_P magnet pole pitch (m)
c_S rotor slot pitch (m)
d_a mean length of the air gap (m)
d_F mean length of path through ferrous material (m)
d_m mean depth of permanent magnet (m)
d_S effective slot depth (m)
e induced electro-magnetic voltage (Volts)
i current value of armature coil (Amp)
k_c Carter's coefficient
l_m axial length of the permanent magnet (m)
l_r axial length of the rotor (m)
p instantaneous power (Watt)
r armature resistance of coil
r_m distance from inside PM surface to rotational axis (m)
r_r distance from rotor surface to rotational axis (m)
tol manufacturer specified tolerance (m)
w_s rotor slot width (m)
α_2 magnitude of air gap oscillation from PM spacing (m)
α_3 magnitude of air gap oscillation from rotor slots (m)
α_4 magnitude of air gap oscillation from eccentricities (m)
α_m distance between rotor surface and inner PM surface (m)
α_r distance from rotor surface to rotational axis of motor (m)
γ_m magnet fraction
λ flux linkage of armature coil (Weber)
λ_{PM} flux linkage of the permanent magnet (Weber)
μ_F permeability of the ferrous material (H/m)
μ_m permeability of the permanent magnet (H/m)
μ_o permeability of air, $4\pi \times 10^{-7}$ (H/m)
μ_R recoil permeability of the permanent magnet
ϕ magnetic flux of armature coil (Weber)
ϕ_{PM} magnetic flux of the permanent magnet (Weber)
ϕ_R remanence flux (Weber)
θ angular position of armature coil (radians)

Subscripts

F ferrous motor material
P permanent magnet poles
S rotor slots
a air gap
j corresponding to a coil from 1 to B
m permanent magnet
r rotor

MODELING

The PMDC motor is modeled through a coupled relationship between the electrical and mechanical subsystems where the electrical subsystem can be modeled by a detailed Kirchhoff loop equation given as

$$V_m = \sum_{j=1}^{B} r_j i_j + \sum_{j=1}^{B} \frac{d}{dt} \lambda_j \quad (1)$$

where V_m is the armature voltage, r_j is the armature resistance, of coil j, i_j is coil j's current value, λ_j is the flux linkage of coil j, and B is the number of coils in the armature.

ElectroMagnetic Flux

The flux linkage λ_j of a coil is the total flux linked through a winding. In Fig. 1 the flux of the circuit passes through each turn of the winding and is defined as

$$\lambda_j = N_j \phi_j \quad (2)$$

where ϕ is the magnetic flux and N is the number of turns in the coil. Each coil in the armature will be associated with a flux linkage equation. The flux of each coil can be calculated by using a standard magnetic circuit shown in Fig.1. Assuming a linear magnetic system and no saturation, the electromagnetic flux ϕ, generated by exciting a coil of N turns with electric current i can be written as

$$\phi = \frac{Ni}{R} \quad (3)$$

where R is the reluctance of the material in Ampere per Weber (A/Wb) or Henries^{-1} (H^{-1}). In a PMDC motor three types of magnetic flux are present. The first type is called *self-induced flux*, which is produced by the current flowing in a coil, which the flux is associated with. The second type of flux is a *mutually induced flux*, also referred to as a magnetizing flux, which is induced in a coil by current flowing in an adjacent coil. The third type of magnetic flux is the *leakage flux*. Because it is a localized flux, *leakage flux* is not seen throughout the magnetic circuit. This flux will not be included in the model presented here because it represents such a small percentage of the total flux. Figure 2 shows a doubly excited magnetic circuit that contains paths for self and mutually induced flux, where the self-induced flux of coil '*a*' is denoted by ϕ_{aa} and the mutually induced flux on coil '*a*' by the current in coil '*b*' is denoted by ϕ_{ab}. Self and mutually induced flux associated with coil j induced by coil j and coil k are

$$\phi_{jj} = \frac{N_j i_j}{R_j} \quad (4)$$

and

$$\phi_{jk} = \frac{N_j i_k}{R_k} \quad (5)$$

respectively. The total flux produced in each coil can now be represented as

$$\lambda_j = \sum_{k=1}^{B} N_j \phi_{jk} + \lambda_{PMj} \quad (6)$$

where the flux linkage of the permanent magnet λ_{PM} is

$$\lambda_{PMj} = N_j \phi_{PM}$$

and ϕ_{PM} is the permanent magnet flux. The combination of Eqs. 4, 5, and 6 results in

$$\lambda_j = \sum_{k=1}^{B} \frac{N_j N_k}{R_k} i_k + \lambda_{PMj} \tag{7}$$

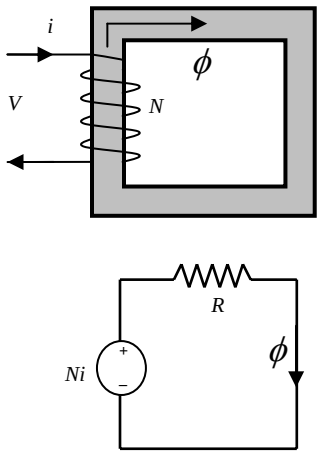

FIGURE 1: EXAMPLE OF SINGLE COIL MAGNETIC CIRCUIT.

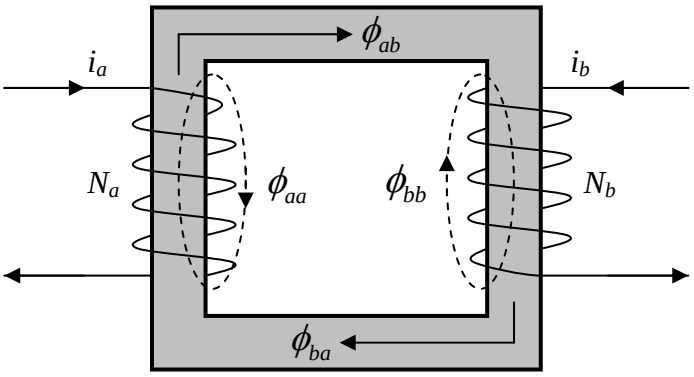

FIGURE 2: DOUBLY EXCITED MAGNETIC CIRCUIT ILLUSTRATING MAGNETIC FLUX TYPES.

Inductance

The results of Eq. 7 show that the magnetic flux of an individual coil is directly proportional to the current in each of the adjacent coils. It is common in a brushed PMDC motor that all the windings have the same number of turns, *N*. Therefore, the individual terms in Eq. 7 can be combined ($N_j = N$, for all j) into a self inductance term,

$$L_j = \frac{N^2}{R_j} \tag{8}$$

and a mutual inductance term,

$$M_{jk} = \frac{N^2}{R_k} \tag{9}$$

With the use of Eqs. 8 and 9 Eq. 7 can be rewritten as

$$\lambda_j = L_j i_j + \sum_{\substack{k=1 \\ k \neq j}}^{B} M_{jk} i_k + \lambda_{PMj} \tag{10}$$

The reluctance related to the coil of a brushed PMDC motor can be written as

$$R = \frac{d_F}{\mu_F A_F} + \frac{d_a}{\mu_o A_a} + \frac{d_m}{\mu_m A_m} \tag{11}$$

where the permanent magnet permeability μ_m is defined as

$$\mu_m = \mu_R \mu_o \tag{12}$$

The recoil permeability μ_R typically has a range of 1.0 to 1.1 and will be given a value of 1.1 in this study. In a PMDC motor, the flux path consists of the rotor, the air gap, the magnetic material, and the motor case. In this path, ferrous materials are used to construct the stator, the rotor, and the permanent magnet. The permeability of air μ_o is at least four orders of magnitudes smaller than that of the ferrous materials related to the stator and rotor. Therefore, for similar geometry we can ignore the effect of the reluctance due to the ferrous materials of the stator and the rotor. The value of the reluctance will vary and subsequently causes changes in inductance. For a given motor during operation, the reluctance varies with the air gap d_a due to rotor eccentricity and the complex geometry of the rotor slots.

Air Gap

Figure 3 shows an example of a slotted rotor and magnetic stator of a PMDC motor. The slots in the rotors cause a change in the distance of the air gap, i.e. the distance between the surface of the magnet and the rotor surface. The change in air gap distance occurs as the rotor rotates, causing the inductance value to vary as a function of the rotor position. Another factor in the variation of the air gap distance is any existing eccentricities due to tolerances in the assembly process. The effect of the eccentricity can be modeled as a sinusoidal fluctuation in the air gap distance seen once per revolution at low or no load conditions.

The air gap distance between the rotor and the magnet is a function of the surface profile of both the rotor and the magnets. Let $r_r(\theta)$ represent the distance of the rotor surface to the rotational axis of the motor and $r_m(\theta)$ represent the distance from the inside magnet surface to the rotational axis of the motor, the resulting air gap, $d_a(\theta)$, is

$$d_a(\theta) = r_m(\theta) - r_r(\theta) \tag{13}$$

Figure 4 illustrates the relative distance from the axis of rotation for the magnet surface and rotor surface as a function of θ if a PMDC motor were cut and unwrapped. Although the actual geometries of the magnet and rotor slots are complicated, sinusoidal profiles are good first order approximations, i.e. let

$$r_m(\theta) = \alpha_m + \alpha_2 \cos(N_P \theta) \tag{14}$$

and

$$r_r(\theta) = \alpha_r + \alpha_3 \cos(N_S \theta) + \alpha_4 \cos(\theta) \tag{15}$$

Substituting Eqs. 14 and 15 into Eq. 13 and simplifying results in

$$d_a(\theta) = \alpha_1 + \alpha_2 \cos(N_P \theta) - \alpha_3 \cos(N_S \theta) - \alpha_4 \cos(\theta) \tag{16}$$

where $\alpha_1 = \alpha_m - \alpha_r$.

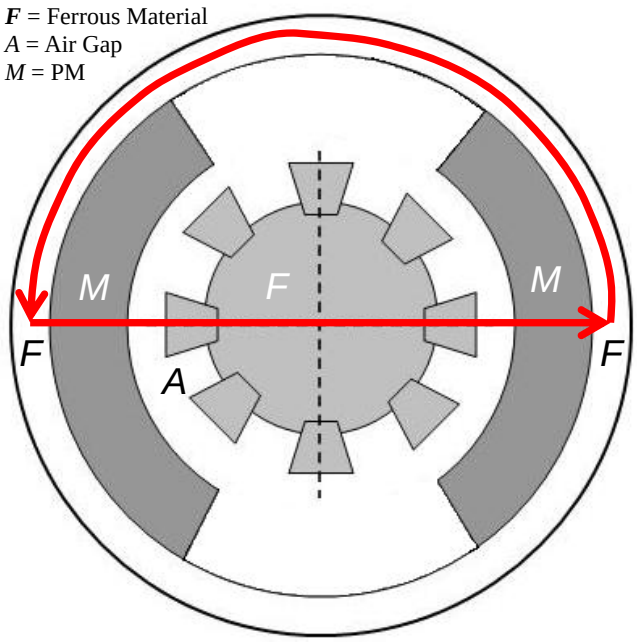

FIGURE 3: MEAN MAGNETIC FLUX FLOW THROUGH A PMDC MOTOR.

Since the air gap $d_a(\theta)$ affects the mean magnet path d in the reluctance, see Eq. 13, the effective reluctance will also be a function of angle θ, i.e. $R(\theta)$. From the reluctance, the dependence on θ will transcend into the flux linkage making the flux linkage a function of the angular position, i.e. Eq. 10 can be written as

$$\lambda_j(\theta,i) = L_j(\theta) i_j + \sum_{\substack{k=1 \\ k\neq j}}^{B} M_{jk}(\theta) i_k + \lambda_{PMj}(\theta) \tag{17}$$

where

$$L_j(\theta) = \frac{N^2}{R_j} = \frac{N^2}{\left(\frac{d_a(\theta_j)}{\mu_o A_a} + \frac{d_m}{\mu_m A_m}\right)} \tag{18}$$

and

$$M_{jk}(\theta) = \frac{N^2}{R_k} = \frac{N^2}{\left(\frac{d_a(\theta_k)}{\mu_o A_a} + \frac{d_m}{\mu_m A_m}\right)} \tag{19}$$

The equation for the flux of the permanent magnet is basically the remanence flux, ϕ_r [14] of the permanent magnet multiplied by a reluctance factor $\frac{R_a}{R_a + R_m}$ that represents the reduction of the remanence flux of the permanent magnet due to the air gap, i.e.

$$\lambda_{PMj}(\theta) = N\phi_{PM} = \frac{NR_a}{(R_a + R_m)}\phi_r = \frac{N\left(\frac{d_a(\theta_j)}{\mu_o A_a}\right)}{\left(\frac{d_a(\theta_j)}{\mu_o A_a} + \frac{d_m}{\mu_m A_m}\right)}\phi_r \tag{20}$$

Detailed equations for the self inductance, mutual inductance, and permanent magnet flux can be derived by inserting Eq. 16 and results in

$$L_j(\theta) = \frac{N^2 \mu_R \mu_o A_m A_a}{\left(\left(\alpha_1 + \alpha_2 \cos(N_P\theta_j) - \alpha_3 \cos(N_S\theta_j) - \alpha_4 \cos(\theta_j)\right)\mu_R A_m + d_m A_a\right)} \tag{21}$$

$$M_{jk}(\theta) = \frac{N^2 \mu_R \mu_o A_m A_a}{\left(\left(\alpha_1 + \alpha_2 \cos(N_P\theta_k) - \alpha_3 \cos(N_S\theta_k) - \alpha_4 \cos(\theta_k)\right)\mu_R A_m + d_m A_a\right)} \tag{22}$$

and

$$\lambda_{PMj}(\theta) = \frac{N\left(\alpha_1 + \alpha_2 \cos(N_P\theta_j) - \alpha_3 \cos(N_S\theta_j) - \alpha_4 \cos(\theta_j)\right)\mu_R A_m \phi_r}{\left(\left(\alpha_1 + \alpha_2 \cos(N_P\theta_j) - \alpha_3 \cos(N_S\theta_j) - \alpha_4 \cos(\theta_j)\right)\mu_R A_m + d_m A_a\right)} \tag{23}$$

where

$$a\theta_j = a\left(\theta + \frac{j}{B} 2\pi\right)$$

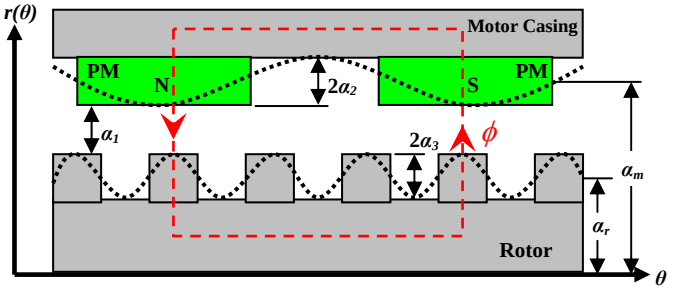

FIGURE 4: APPROXIMATED OSCILLATIONS OF THE AIR GAP BASED ON ANGULAR POSITION Θ.

Electro-Magnetic Characteristics

The flux linkage induces a back EMF voltage across the coils of the armature whenever the flux linkage varies with time as stated by Faraday's Law. Applying Faraday's Law to Eq. 17 gives

$$\frac{d\lambda_j(\theta,i)}{dt} = L_j(\theta)\frac{di_j}{dt} + \sum_{\substack{k=1 \\ k\neq j}}^{B} M_{jk}(\theta)\frac{di_k}{dt} + \frac{d\theta}{dt}\left(\frac{dL_j(\theta)}{d\theta} i_j + \sum_{\substack{k=1 \\ k\neq 1}}^{B} \frac{dM_{jk}(\theta)}{d\theta} i_k + \frac{d\lambda_{PMj}(\theta)}{d\theta}\right) \tag{24}$$

The first two terms on the right hand side of Eq. 24 capture the typical voltage across the inductance. The derivatives of the

self and mutual inductances and the permanent magnet flux with respect to the angular position are

$$\frac{dL_j(\theta)}{d\theta}=\frac{N^2\mu_R^2A_m^2\mu_oA_a\left(N_P\alpha_2\sin\left(N_P\theta_j\right)-N_S\alpha_3\sin\left(N_S\theta_j\right)-\alpha_4\sin\left(\theta_j\right)\right)}{\left(\left(\alpha_1+\alpha_2\cos\left(N_P\theta_j\right)-\alpha_3\cos\left(N_S\theta_j\right)-\alpha_4\cos\left(\theta_j\right)\right)\mu_RA_m+d_mA_a\right)^2} \tag{25}$$

$$\frac{dM_{jk}(\theta)}{d\theta}=\frac{N^2\mu_R^2A_m^2\mu_oA_A\left(N_P\alpha_2\sin\left(N_P\theta_k\right)-N_S\alpha_3\sin\left(N_S\theta_k\right)-\alpha_4\sin\left(\theta_k\right)\right)}{\left(\left(\alpha_1+\alpha_2\cos\left(N_P\theta_k\right)-\alpha_3\cos\left(N_S\theta_k\right)-\alpha_4\cos\left(\theta_k\right)\right)\mu_RA_m+d_mA_a\right)^2} \tag{26}$$

and

$$\frac{d\lambda_{PMj}(\theta)}{d\theta}=\frac{Nd_mA_mA_a\mu_R\phi_r\left(N_P\alpha_2\sin\left(N_P\theta_j\right)-N_S\alpha_3\sin\left(N_S\theta_j\right)-\alpha_4\sin\left(\theta_j\right)\right)}{\left(\left(\alpha_1+\alpha_2\cos\left(N_P\theta_j\right)-\alpha_3\cos\left(N_S\theta_j\right)-\alpha_4\cos\left(\theta_j\right)\right)\mu_RA_m+d_mA_a\right)^2} \tag{27}$$

The last term in Eq. 24 is also known as the back EMF voltage and is proportional to the angular velocity of the motor. A back EMF factor can be derived as

$$K_v(\theta)=\sum_{j=1}^{B}\left(\frac{dL_j(\theta)}{d\theta}i_j+\sum_{\substack{k=1\\k\neq j}}^{B}\frac{dM_{jk}(\theta)}{d\theta}i_k+\frac{d\lambda_{PM}(\theta)}{d\theta}\right) \tag{28}$$

The voltage loop equation, Eq. 1, can now be written as

$$\begin{aligned}V_m&=\sum_{j=1}^{B}r_ji_j+\sum_{j=1}^{B}\left(L_j(\theta)\frac{di_j}{dt}_j+\sum_{\substack{k=1\\k\neq j}}^{5}M_{jk}(\theta)\frac{di_k}{dt}\right)\\&\quad+\frac{d\theta}{dt}\sum_{j=1}^{B}\left(\frac{dL_j(\theta)}{d\theta}i+\sum_{\substack{k=1\\k\neq j}}^{B}\frac{dM_{jk}(\theta)}{d\theta}i_k+\frac{d\lambda_{PM}(\theta)}{d\theta}\right)\\&=\sum_{j=1}^{B}r_ji_j+\sum_{j=1}^{B}\left(L_j(\theta)\frac{di_j}{dt}_j+\sum_{\substack{k=1\\k\neq j}}^{B}M_{jk}(\theta)\frac{di_k}{dt}\right)\\&\quad+K_v(\theta)\frac{d\theta}{dt}\end{aligned} \tag{29}$$

This equation provides a more comprehensive model for the armature coil voltage in a PMDC motor. For a serially wound armature winding, the currents in all the coils are identical, i.e. $i_j = i$, for $i = 1,\ldots, B$, Eq. 29 can be further simplified to

$$\begin{aligned}V_m&=\sum_{j=1}^{B}r_ji+\left[\sum_{j=1}^{B}\left(L_j(\theta)+\sum_{\substack{k=1\\k\neq j}}^{B}M_{jk}(\theta)\right)\right]\frac{di}{dt}+K_v(\theta)\frac{d\theta}{dt}\\&=Ri+L(\theta)\frac{di}{dt}+K_v(\theta)\frac{d\theta}{dt}\end{aligned} \tag{30}$$

Torque Generation

The output torque of a PMDC motor can be derived through the energy in the magnetic field. In order to calculate the energy in the magnetic field instantaneous power of the motor is needed. This power can be seen as

$$p=vi=ri^2+ei \tag{31}$$

where v is the input voltage, i is the total armature current, r is the total resistance , and e is the induced electro-magnetic voltage. The power input to the motor can be split into two parts: the first being dissipated as a resistive loss and the second will become stored energy in the rotor field. Only the stored energy is capable of producing torque. The differential electrical-input energy can be written as, [15]

$$\begin{aligned}dW_{elec}&=eidt\\&=\sum_{j=1}^{B}\left(\begin{array}{l}L_j(\theta)idi+i\sum_{\substack{k=1\\k\neq j}}^{B}M_{jk}(\theta)di+\\\left(\begin{array}{l}\frac{dL_j(\theta)i^2}{+i^2\sum_{\substack{k=1\\k\neq j}}^{B}dM_{jk}(\theta)}\\+id\lambda_{PMj}(\theta)\end{array}\right)\end{array}\right)\end{aligned} \tag{32}$$

Conservation of energy in an electro-mechanical machine states that the total input energy is either stored in the electromagnetic field or in the form of mechanical energy by doing work, i.e.

$$dW_{elec}=dW_f+T_Dd\theta \tag{33}$$

where W_{elec} is defined as the total stored energy, W_f is the energy stored in the electromagnetic field, and $T_Dd\theta$ is the output mechanical energy (N-m). To determine an expression for energy stored in the magnetic field W_f, the rotor will be assumed be held at a fixed angle. This results in $d\theta = 0$, along with all the derivatives of $d\theta$ in dW_{elec}. This assumption simplifies the change in total stored energy to

$$dW_{elec}=\sum_{j=1}^{B}\left(L_j(\theta)+\sum_{\substack{k=1\\k\neq j}}^{B}M_{jk}(\theta)\right)\cdot i\,di \tag{34}$$

By assuming that the rotor is held in a fixed position the third term in Eq. 33 becomes zero and at this instant the stored energy in the magnetic field can be written as

$$W_f=\int dW_{elec}=\frac{1}{2}\sum_{j=1}^{B}\left(L_j(\theta)+\sum_{\substack{k=1\\k\neq j}}^{B}M_{jk}(\theta)\right)\cdot i^2 \tag{35}$$

and

$$dW_f=\sum_{j=1}^{B}\left(\frac{1}{2}dL_j(\theta)i^2+L_j(\theta)i+\frac{1}{2}i^2\sum_{\substack{k=1\\k\neq j}}^{B}dM_{jk}(\theta)+i\sum_{\substack{k=1\\k\neq j}}^{B}M_{jk}(\theta)\right) \tag{36}$$

The developed torque T_D can then be derived by substituting Eqs. 32 and 35 into Eq. 33 resulting in

$$T_D=\sum_{j=1}^{B}\left(\frac{1}{2}\frac{dL_j(\theta)}{d\theta}i^2+\frac{1}{2}\sum_{\substack{k=1\\k\neq j}}^{B}\frac{dM_{jk}(\theta)}{d\theta}i^2+\frac{d\lambda_{PM}(\theta)}{d\theta}i\right) \tag{37}$$

which can also be written as

$$T_D=\sum_{j=1}^{B}\left(\frac{1}{2}\frac{dL_j(\theta)}{d\theta}i^2+\frac{1}{2}\sum_{\substack{k=1\\k\neq j}}^{B}\frac{dM_{jk}(\theta)}{d\theta}i^2+\frac{d\lambda_{PMj}(\theta)}{d\theta}i\right)=K_Ti+TR \tag{38}$$

where the total torque can be divided into the nominal developed torque $K_T i$ and the TR.

EXPERIMENTAL VERIFICATION AND SENSITIVITY ANALYSIS

Motors from four different motor vendor manufacturers were used to verify the model derived above. These manufacturers were given identical motor specifications, which can be seen in Table 1.

TABLE 1: PMDC MOTOR SPECIFICATIONS GIVEN TO VENDORS.

c_p

Mechanical Specifications	Motor Length (mm)	50
	Motor Diameter (mm)	38.5
	Rotor Inertia (g-cm^2)	35
Electrical Specifications	Max Cogging Torque (N-cm)	0.7
	Terminal Resistance (Ω)	6.8
	Terminal Inductance (mH)	9.2
Motor Performance Specifications	Torque Constant (N-cm/Amp)	4.8
	No Load Speed (rpm)	3400
	Stall Torque (N-cm)	12.2

Modeling Parameters

Modeling parameters needed to calculate T_D in Eq. 37 can be measured from the physical motors obtained from vendors. Figures 5 through 7 illustrate parameters measured from the motors. These physical parameters can be used to calculate variable such as the cross-sectional air gap A_a which can be defined as

$$A_a = \frac{c_p\left(l_R + \gamma_m l_m\right)}{2} \tag{39}$$

where γ_m is the ratio of c_m to c_p. The modeling parameters related to air gap oscillations are estimated through physical parameters since they can not be directly measured. In order to calculate α_1, the distance from the rotational axis to the outside radius r_r of the rotor was measured and then the distance from the rotational axis to the inside radius of the PM r_m was measured. The value of α_1 is then defined as the difference of these two values. The value of α_2 can be determined by first measuring the depth of the PM d_m and then multiplying by one-half. α_3 is defined as half of the rotor slot depth d_s. Since the rotor slots have different geometry, an approximation of the slot depth will be used. The flux will seek the path of least resistance implying that flux that enters a slot will start to curve toward the closest tooth in order to reduce reluctance. To find the effective slot depth, the Carter's coefficient [14] will be used to approximate the effective slot depth d_s based on the slot width w_s, and the slot pitch c_s, see Fig. 6, where d_s is equal to

$$d_s = \left|1 - k_c\right|\alpha_1 \tag{40}$$

α_4 was approximated to be half of ten percent of the eccentricity tolerance specified for the motor or

$$\alpha_4 = \tfrac{1}{2}\left(0.1 * tol\right) \tag{41}$$

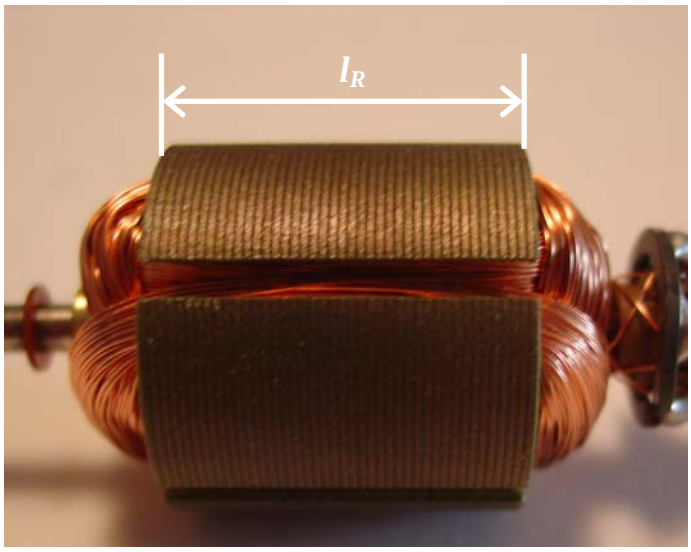

FIGURE 5: AXIAL PARAMETERS OF A PMDC MOTOR.

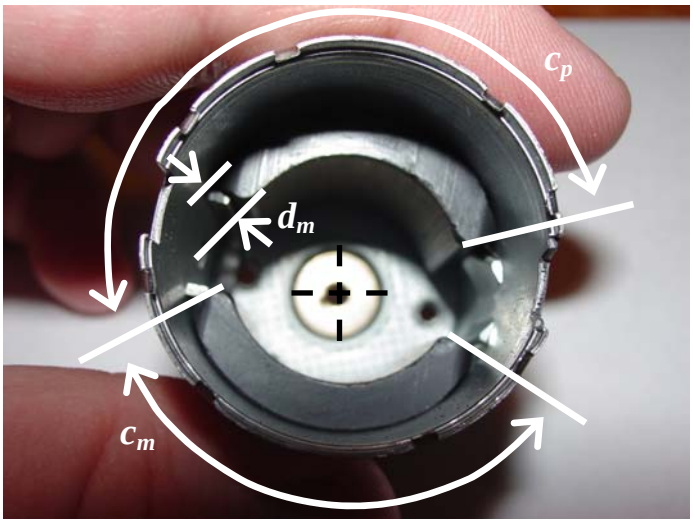

FIGURE 6: RADIAL PARAMETERS RELATED TO PM GEOMETRIES.

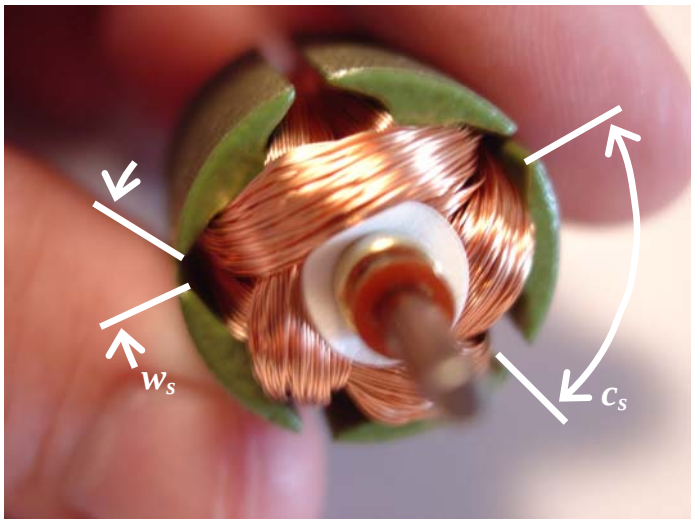

FIGURE 7: RADIAL PARAMETERS RELATED TO ROTOR GEOMETRIES.

The parameters related to the geometrical shape of the permanent magnet consist of the cross-sectional area of the magnet A_m, magnet depth d_m, and the permeability of the magnet μ_m. The cross-sectional area of the magnet can be calculated as

$$A_m = \gamma_m l_m \tag{42}$$

Simulation Results

To verify the analytical model, *TR* was experimentally measured along with the corresponding armature current. The measurement of *TR* was done on a test stand that was developed for this specific purpose [16]. The test stand was designed to take a voltage and a load specified by the user. The tests were run until a specified number of data points had been collected. This test stand is unique in that it will maintain the desired voltage through observer control. Once the test was completed the mean of the measured torque value was computed and then subtracted from the measured torque value to determine *TR*

In order to simulate T_D and *TR*, measured parameters were used in Eq. 37 along with measured armature current taken for each vendor. Identical data processing procedures were used on both the experimental and simulation data.

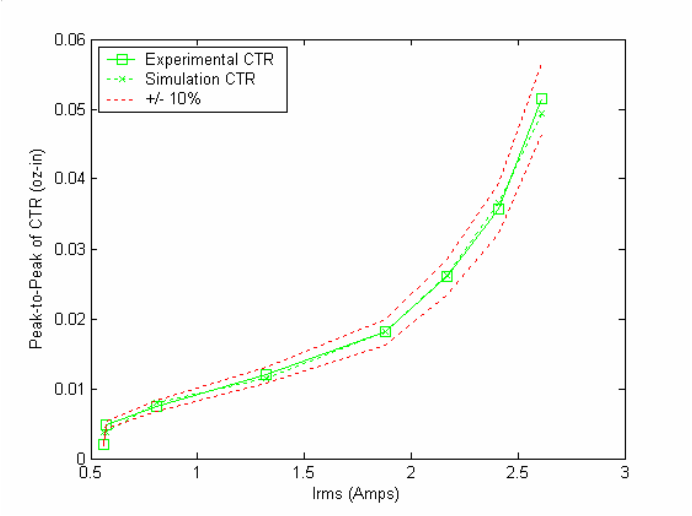

FIGURE 8: COMPARISON OF *TR* GROWTH FROM EXPERIMENTAL AND SIMULATION RESULTS COLLECTED FROM VENDOR A.

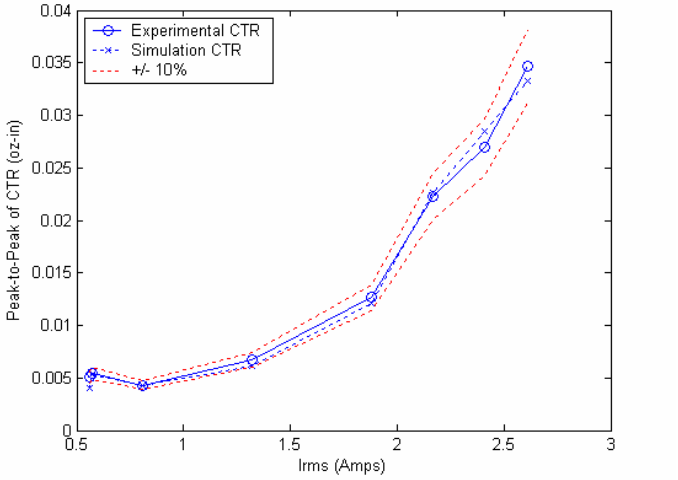

FIGURE 9: COMPARISON OF *TR* GROWTH FROM EXPERIMENTAL AND SIMULATION RESULTS COLLECTED FROM VENDOR B.

Figures 8 through 11 show comparisons of the *TR* magnitudes as a function of the RMS armature current value between the model estimation and the actual experimental data for all of the four vendors. The figures show the experimental growth, solid line, of *TR* over various loads compared to the simulation results, dashed line. The figures also contain two dashed lines placed at $\pm 10\%$ of the experimental growth. The *TR* magnitude is defined to be the peak to peak value of the *TR* for a complete revolution, i.e.

$$TR \text{ Magnitude} = \max_k(TR(k)) - \min_k(TR(k)) \tag{43}$$

These figures prove that the simulation can provide accurate estimates of the *TR*'s magnitude and growth over a range of armature current values.

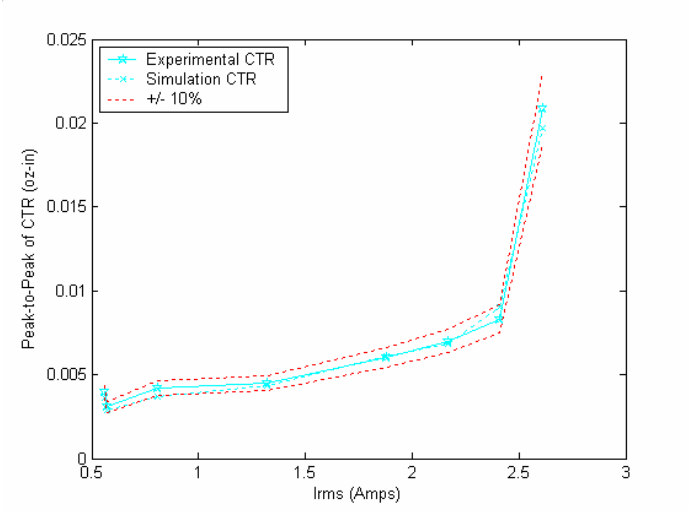

FIGURE 10: COMPARISON OF *TR* GROWTH FROM EXPERIMENTAL AND SIMULATION RESULTS COLLECTED FROM VENDOR C.

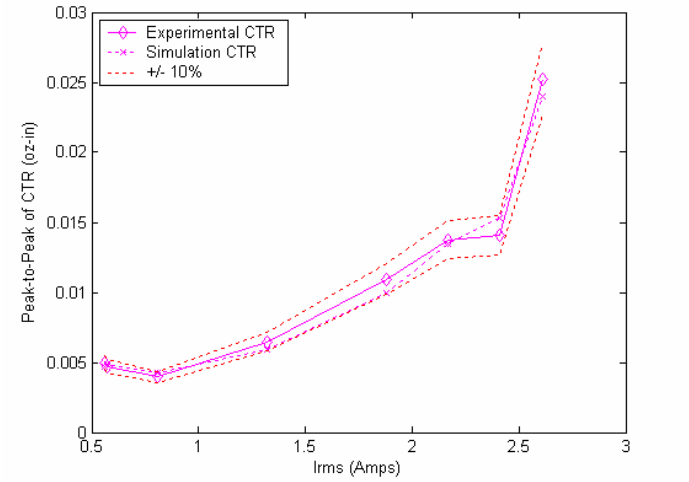

FIGURE 11: COMPARISON OF *TR* GROWTH FROM EXPERIMENTAL AND SIMULATION RESULTS COLLECTED FROM VENDOR D.

Sensitivity Analysis

Sensitivity analysis was performed on the *TR* in order to determine which parameter used in the calculation of Eq. 37 caused the highest % change in *TR*. Table 2 provides the numerical results for the sensitivity analysis. The results show that α_2 has the largest percent sensitivity change affect on *TR*. The parameter α_2 is related to the magnitude of d_m so the magnet depth is really the most influential parameter. After the magnet depth, the length of the rotor and number of turns in the coil play a considerable role in the torque production. The length of the magnet l_m, the length of the rotor l_r, the parameters α_3 and α_2 are the key parameters with respect to *TR*. The length of the magnet and that of the rotor are usually constrained by the available space around the motor so these parameters might not be as flexible in the design process and should be thought of as more critical to T_D.

TABLE 2: NUMERICAL RESULTS OF SENSITIVITY ANALYSIS PERFORMED ON PARAMETERS RELATED TO *TR*.

Parameters	Vendor A	Vendor B	Vendor C	Vendor D
N	4.83	4.50	6.74	6.57
μ_m	4.60	4.07	4.17	4.30
l_m	8.56	7.47	8.12	8.17
l_R	9.08	8.13	9.98	9.83
d_m	5.37	4.91	6.75	6.89
c_p	6.99	6.14	7.32	7.65
c_m	7.14	6.19	7.47	7.71
ϕ_r	7.15	6.35	8.13	8.34
α_1	4.83	4.31	5.24	5.08
α_2	11.35	10.15	9.31	10.18
α_3	8.01	7.14	8.47	8.73
α_4	7.30	6.59	7.74	8.01

CONCLUSION

The analytical model was verified through comparison with experimental data with four vendors with the results being contained within a 10% bound. Results of a sensitivity analysis determined that magnet depth was the most influential physical parameter related to the magnitude of torque ripple. After this the length of the armature, the length of the magnet, and the effective rotor slot depth were determined to also be highly correlated to torque ripple. A reduction in any of these parameters will not only reduce the magnitude of the torque ripple but also the developed torque. While a reduction in the magnitude of the torque ripple is desired, a reduction of the output torque is not. These parameters can be used to optimize the motor design by maximizing the output torque while minimizing the associated torque ripple.

REFERENCES

[1] Ree, J. D. L., and Boules, N., 1989, "Torque Production in Permanent-Magnet Synchronous Motors", IEEE Transactions on Industry Applications, 25(1), pp. 107-112.

[2] Zhu, Z. Q., and Howe, D., 1992, "Analytical Prediction of the Cogging Torque in Radial-field Permanent Magnet Brushless Motors", IEEE Transactions on Magnetics, 28(2), pp 1371-1374.

[3] Ackermann, B., Janssen, J. H. H., Sottek, R., and van Steen, R. I., 1992, "New Technique for Reducing Cogging

Torque in a Class of Brushless DC Motors", IEEE Proceedings-B, 139(4), pp. 315-320.
[4] Deodhar, R. P., Staton, D. A., and Miller, T. J. E., 1996, "Modeling of Skew using the Flux-MMF Diagram [of PM Machines]", IEEE Transactions on Industry Applications, 32(6), pp. 1339-1347.
[5] Hwang, S., and Lieu, D. K., 1994, "Design Techniques for Reduction of Reluctance Torque in Brushless Permanent Magnet Motors", IEEE Transactions on Magnetics, 30(6), pp. 4287-4289.
[6] Hanselman, D., 1997, "Effect of Skew, Pole Count, and Slot Count on Brushless Motor Radial Force, Cogging Torque, and Back EMF", IEE Proceedings on Electrical Power Applications, 144(5), pp. 325-330.
[7] Li, T., and Slemon, G., 1988, "Reduction of Cogging Torque in Permanent Magnet Motors", IEEE Transactions on Magnetics, 24(6), pp. 2901-2903.
[8] Ishikawa, T., and Slemon, G., 1993, "A Method of Reducing Ripple Torque in Permanent Magnet Motors without Skewing", IEEE Transactions on Magnetics, 29(2), pp. 2028-2031.
[9] Bianchi, N., and Bolognani, S., 2002, "Design Techniques for Reducing the Cogging Torque in Surface-Mounted PM Motors", IEEE Transactions on Industry Applications, 38(5), pp. 1259-1265.
[10] Miller, T. and Rabinovici, R., 1994, "Back-EMF Waveforms and Core Losses in Brushless DC Motors", IEE Proceedings on Electrical Applications, 141(3), pp. 144-154.
[11] Hanselman, D., 1994, "Minimum Torque Ripple, Maximum Efficiency Excitation of Brushless Permanent Magnet Motors", IEEE Transactions on Industrial Electronics, 41(3), pp. 292-300.
[12] Murray, A., 1993, "Torque and EMF Ripple Reduction in Brushless Machines", IEE Colloquium on Permanent Magnet Machines and Drives.
[13] Boules, N., 1990, "Design Optimization of Permanent Magnet DC Motors", IEEE Transactions on Industry Applications, 26(4), pp. 786-792.
[14] Hanselman, D. C., 1994, *Brushless Permanent-Magnet Motor Design*, McGraw-Hill, New York.
[15] McPherson, G., and Laramore, R. D., 1981, *An Introduction to Electrical Machines and Transformers*, John Wiley and Sons, New York.
[16] Howard, D., 2004, "Observer Based Commutation Torque Estimation in Brushed Permanent Magnet Direct Current Motors, Masters Thesis, Purdue University, West Lafayette, IN.